Distinct crustal isostasy trends east and west of the Rocky Mountain Front

Brandon Schmandt[1], Fan-Chi Lin[2], and Karl E. Karlstrom[1]

[1]Earth and Planetary Sciences Department, University of New Mexico, Albuquerque, New Mexico, USA, [2]Department of Geology and Geophysics, University of Utah, Salt Lake City, Utah, USA

Abstract Seismic structure beneath the contiguous U.S. was imaged with multimode receiver function stacking and inversion of Rayleigh wave dispersion and ellipticity measurements. Crust thickness and elevation are weakly correlated across the contiguous U.S., but the correlation is ~3–4 times greater for separate areas east and west of the Rocky Mountain Front (RMF). Greater lower crustal shear velocities east of the RMF, particularly in low-elevation areas with thick crust, are consistent with deep crustal density as the primary cause of the contrasting crust thickness versus elevation trends. Separate eastern and western trends are best fit by Airy isostasy models that assume lower crust to uppermost mantle density increases of $0.18 \, g/cm^3$ and $0.40 \, g/cm^3$, respectively. The former value is near the minimum that is plausible for felsic lower crust. Location of the transition at the RMF suggests that Laramide to post-Laramide processes reduced western U.S. lower crustal density.

1. Introduction

Constraining continental crust thickness and seismic velocities provides insight into the sources of buoyancy underlying modern topography, the composition of the deep crust, and the processes of continental assembly and deformation. In the largest active orogens crust thickness and elevation are roughly consistent with the Airy isostasy hypothesis [e.g., *Beck et al.,* 1996], which posits that elevation is compensated by thickness variations of uniform density crust. Many ancient mountain belts also exhibit positive correlations between crust thickness and elevation, but their crustal roots are disproportionately thick for their low modern elevations suggesting postorogenic increases in density [*Fischer*, 2002]. The lower crust to upper mantle density increase required for crustal isostasy in these settings is often $\sim0.1–0.2 \, g/cm^3$ [*Li et al.,* 2002; *Hawman et al.,* 2012]. Similar or smaller density contrasts are possible if the lower crust is rich in mafic cumulates or basalt, but the prevalence of mafic lower crust is unclear because some felsic compositions have density contrasts with the upper mantle as small as $\sim0.15–0.2 \, g/cm^3$ and similar seismic velocities [*Hacker et al.,* 2015]. Isolated regional seismic studies and compilations thereof [e.g., *Christensen and Mooney*, 1995] generally provide the observational basis for hypotheses regarding deep crustal composition and isostasy. Spatially continuous large-scale studies could provide a more systematic perspective.

As a result of EarthScope's USArray deployment of broadband seismometers it is possible to investigate lithospheric structure across the contiguous U.S. with about 70 km horizontal resolution and compare the remnants of ancient orogens to the active western Cordillera. Here we present new images of crustal thickness and seismic shear velocity (V_s) derived from multimode receiver function imaging and Rayleigh wave tomography. Distinct crust thickness versus elevation trends are identified east and west of the Rocky Mountain Front (RMF) and primarily attributed to a contrast in lower crustal density.

2. Data and Methods

2.1. Multimode Receiver Function Imaging

Broadband seismic waveforms were acquired from the Incorporated Research Institutions for Seismology Data Management Center (IRIS DMC) for USArray data up to June 2015 and augmented by temporary array and regional observatory stations for a total of 2835 stations (Figure 1). Teleseismic *P* waveforms were used from earthquakes with $M_w > 5.5$ and distances of 30–90°. The main steps in the multimode receiver function imaging approach were estimation of *P*-to-*S* (*Ps*) receiver functions, mapping of receiver function time to depth for three scattering modes [*Wilson and Aster*, 2005] (see supporting information), and common conversion point (CCP) stacking to form a 3-D image [*Dueker and Sheehan*, 1997; *Angus et al.,* 2009]. Receiver
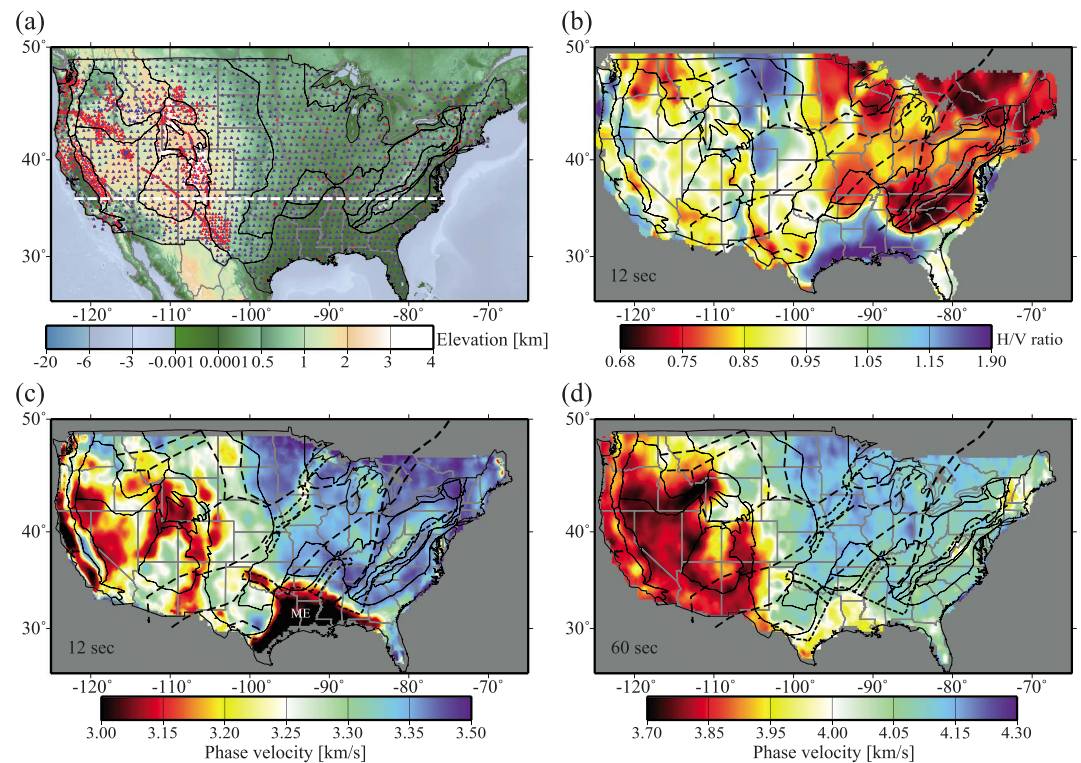
Figure 1. Stations map and Rayleigh wave measurements. (a) Station map with physiographic boundaries [*Fenneman*, 1928]. Stations used for both receiver function and Rayleigh wave imaging are shown as blue triangles and stations used only for receiver functions are red. The white dashed line shows the location of the cross section in Figure 2. (b) Rayleigh wave *H/V* ratio map with dashed lines showing tectonic boundaries following *Whitmeyer and Karlstrom* [2007]. Lines with smaller dashes correspond to rift boundaries and larger dashes correspond to collisional boundaries. (c) Phase velocity map for 12 s period, both physiographic and tectonic boundaries are shown. The Mississippi Embayment (ME) is labeled. (d) Phase velocity map for 60 s period.

functions were estimated with a multichannel source estimation and deconvolution method [*Mercier et al.,* 2006; *Hansen and Dueker*, 2009], expanding upon results of *Schmandt et al.* [2012].

Initial time to depth mapping and CCP imaging used the velocity model from *Schmandt and Lin* [2014], but after the first Rayleigh wave inversion in this study the CCP imaging and Rayleigh wave inversion were repeated so that the final velocity model and crustal thickness map are consistent. The CCP images used a Gaussian weighting function [*Eagar et al.,* 2011] with a half-width of 40 km. For the composite image the polarity of the 2s1p mode was reversed and the three separate mode images were averaged with equal weighting (Figure 2 and the supporting information). Absolute changes in crustal thickness due to updating the velocity model after the first Rayleigh wave inversion averaged 0.7 km and all changes were <3 km. Further iterations were not conducted because all changes would be <1 km.

Lower frequencies were used for the 2p1s and 2s1p mode CCP images, <0.25 Hz, compared to the *Ps* mode, <0.5 Hz. The utility of lower frequencies for free surface multiples is often recognized in scattered wave inversion studies [*Mackenzie et al.,* 2010; *Kim et al.,* 2012], and we found that Moho multiples were more prominent below ~0.3 Hz. Another motivation for using lower frequencies for the 2p1s and 2s1p modes is that it results in more similar Moho pulse widths after the receiver functions are mapped to depth. Using uniform frequency content for the free surface multiples results in depth domain pulse widths that are narrower than for the Ps mode (supporting information).

Estimation of local Moho depths from the CCP images was conducted with initial automated picks followed by a combination of automated and visual refinement to consider information from all three scattering modes (Figure 3a). Initial automated picks were determined by the maximum value in the composite image within 35% of the depth predicted by the Crust1 model [*Laske et al.,* 2013]. A linearly interpolated Moho
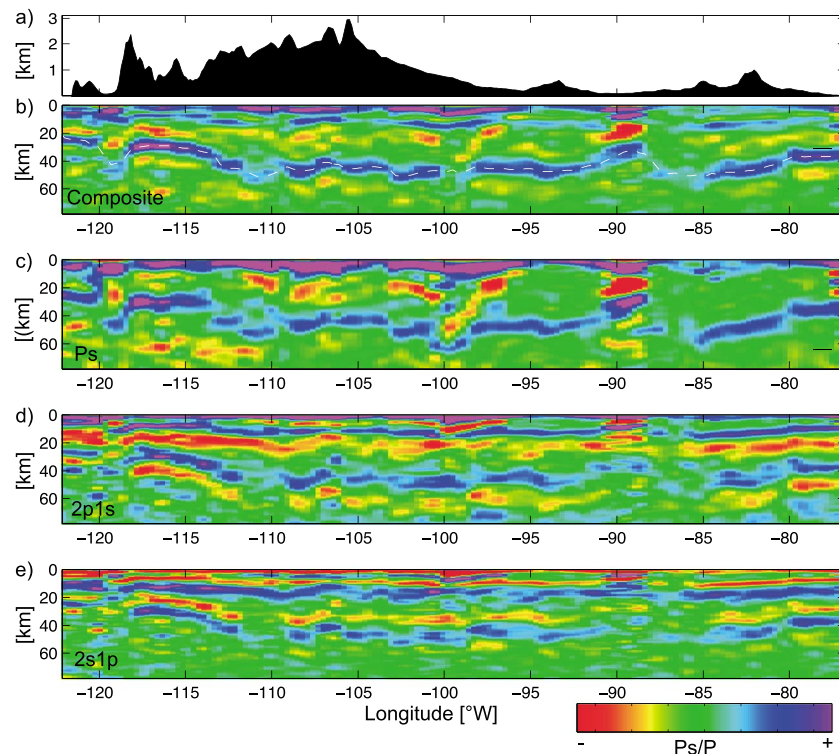
Figure 2. Multimode CCP imaging. (a) Smoothed topography along a latitude of 36°N. (b) Composite CCP image made by averaging the images in Figures 2c–2e, color-scale bounds are ±6%. Estimated Moho depth is shown by the dashed white line. (c) *Ps* mode CCP image with color-scale bounds of ±10%. (d) 2p1s mode CCP image with color-scale bounds of ±10%. (e) 2s1p mode CCP image, same color scale as Figure 2d.

surface was formed using picks at locations where there was no other local maximum with amplitude >50% of the global maximum. For locations with multiple local maxima the maximum nearest to the interpolated surface was selected. Finally, the automated picks were refined by visually culling east-west and north-south cross sections, while viewing CCP images for each mode. An example where the separate mode images are useful is near 36°N, −100°W, where the *Ps* Moho arrival appears to deepen locally beneath the Anadarko basin but the 2p1s and 2s1p modes indicate a flat Moho (Figure 2). Here it is likely that free surface multiples created by the ~5–7 km deep sediment to basement interface [*Blackwell et al.,* 2006] interfere with the *Ps* arrival from the Moho.

2.2. Inversion of Rayleigh Wave Dispersion and Ellipticity Data

All available continuous time series recorded by USArray stations (Figure 1) between January 2007 and February 2015 were cross correlated to obtain multicomponent empirical Green's functions between each station pair [*Bensen et al.,* 2007; *Lin et al.,* 2014]. Eikonal tomography [*Lin et al.,* 2009] was then applied to construct Rayleigh wave phase velocity maps between 8 and 24 s period (Figure 1). For each period and station, the Rayleigh wave ellipticity, or horizontal-to-vertical amplitude ratio (*H/V* ratio), was determined by averaging all available vertical to radial component cross-correlation amplitude ratios for a common receiver [*Lin et al.,* 2014] (Figure 1).

To obtain complementary maps at longer periods, all available teleseismic Rayleigh from earthquakes with $M_s > 5.0$ between January 2007 and May 2015 were used. Helmholtz tomography [*Lin and Ritzwoller,* 2011] was applied to construct Rayleigh wave phase velocity maps between 24 and 100 s period (Figure 1). The phase front tracking results from Helmholtz tomography were used to determine the radial direction for *H/V* ratio measurements. For each station and period, all available *H/V* ratio measurements were averaged to determine the final *H/V* ratio maps between 24 and 100 s period [*Lin et al.,* 2012]. All phase velocity and *H/V* maps were smoothed with a 0.5° Gaussian filter.
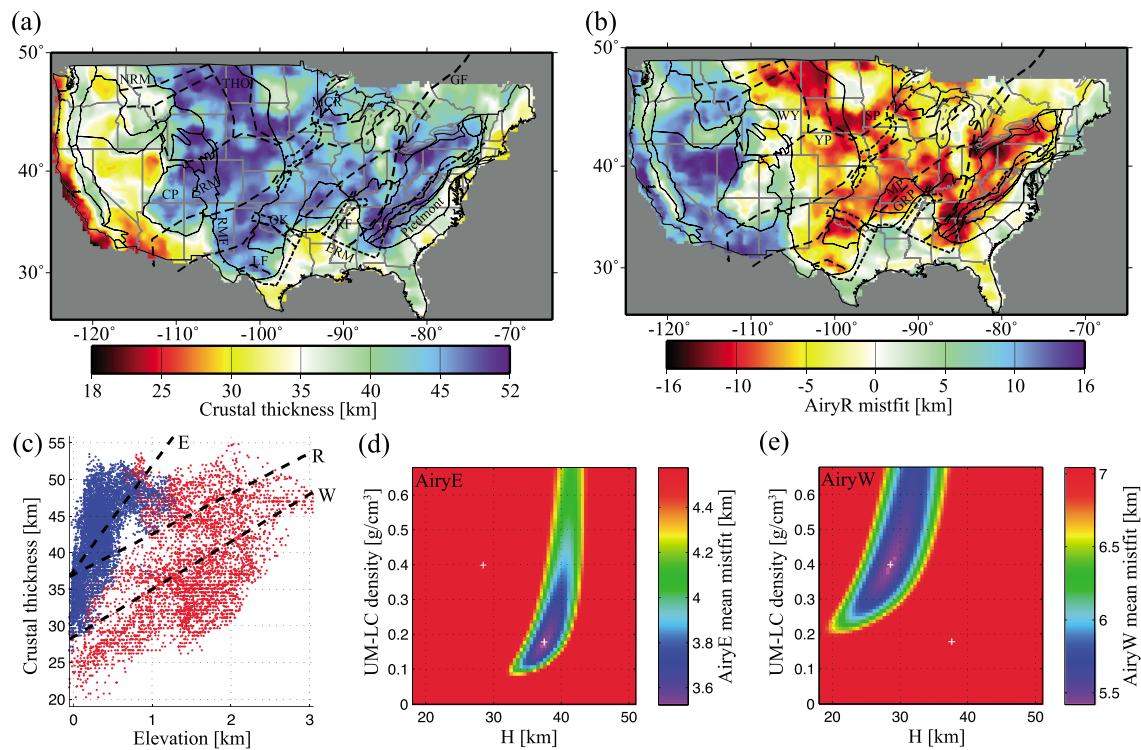
Figure 3. Crust thickness and isostasy models. (a) Crust thickness map with some labeled physiographic provinces (black contours): the Rocky Mountain Front (RMF), northern and southern Rocky Mountains (NRM, SRM), Colorado Plateau (CP), and the Appalachian Piedmont. Labeled tectonic features (black dashed contours) are the Trans Hudson Orogen (THO), Midcontinent Rift (MCR), Oklahoma aulacogen (OK), Reelfoot Rift, Grenville Front (GF), Llano Front (LF), and the Precambrian eastern rift margin (ERM). (b) Map of deviations from the AiryR model prediction. Labeled tectonic provinces are the Wyoming craton (WY), Superior craton (SP), Yavapai Province (YP), Mazatzal Province (MP), Granite-Rhyolite Province (GRP). (c) Crust thickness versus smoothed elevation scatterplot, with black dashed lines for the AiryR, AiryE, and AiryW models. Blue and red dots correspond to points east and west of the RMF, respectively. (d) L1 misfit surface for AiryE, white cross marks the optimal values for AiryE and AiryW. (e) L1 misfit surface for AiryW.

We followed the method described by *Lin et al.* [2014] to jointly invert phase velocity and ellipticity measurements for a 3-D V_s model. At each location on a 0.2° grid, phase velocity and H/V ratio measurements between 8 and 100 s period and crust thickness determined in section 2.1 were used to invert for 1-D V_s models between 0 and 150 km depth. Outstanding depth resolution can be achieved in the crust because of the shallow sensitivity of the H/V ratio measurements [*Tanimoto and Rivera*, 2008]. We used the empirical relationship between V_s, V_p, and density for crustal rocks proposed by *Brocher* [2005] to guide the inversion because only V_s is well constrained deeper than ~15 km. All the inverted 1-D models were combined to obtain the final 3-D V_s model (Figure 4).

2.3. Airy Isostasy Models

We evaluated the Airy isostasy hypothesis for the cumulative study area using global reference values and for separate areas east and west of the RMF. Following *Sheehan et al.* [1995], we calculated an Airy model misfit (AMM) function given by $AMM = H + (\rho_{uc}/\rho_{um} - \rho_{lc})E - ECT$, where H is the crustal thickness at sea level, E is elevation from ETOPO1 smoothed in a 20 km radius [*Amante and Eakins*, 2009], and ECT is estimated crustal thickness from this study. For all three models upper crustal density (ρ_{uc}) of 2.6 g/cm³ was assumed based on preliminary reference Earth model (PREM) [*Dziewonski and Anderson*, 1981]. For the reference Airy model, AiryR, the upper mantle to lower crust density difference ($\rho_{um} - \rho_{lc}$) was set to 0.48 g/cm³ following PREM, and an optimal H of 37 km was found using a grid search parameterized with 0.5 km increments to minimize the L1 norm of AMM. The AiryR misfit is primarily used to illustrate observed deviations from predictions by global reference densities (Figure 3b). Two additional models AiryE and AiryW were created using an L1 grid search to optimize both H and $\rho_{um} - \rho_{lc}$ for the areas east and west of the RMF, respectively. The grid searches used increments of
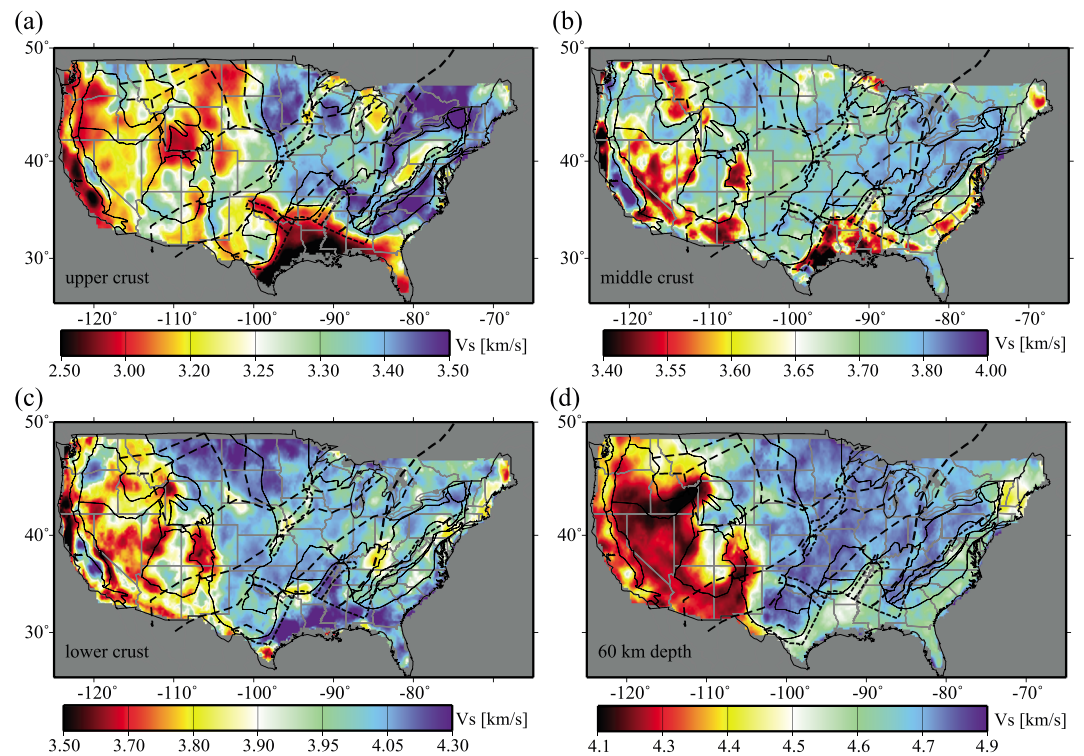
Figure 4. Shear velocity structure. (a) V_s map in the upper crust, 0–11 km. (b) V_s map in the middle crust. (c) V_s map in the lower crust. (d) V_s map in the uppermost mantle at 60 km.

0.01 g/cm^3 for $\rho_{um} - \rho_{lc}$ and 0.5 km for H. The relevant lower crust thickness in this isostasy equation scales with Moho relief relative to H, which varies spatially.

3. Results

3.1. Crust Thickness

Results for the western U.S. are generally consistent with prior studies [*Lowry and Pérez-Gussinyé*, 2011; *Gilbert*, 2012; *Levander and Miller*, 2012; *Shen et al.*, 2013a] and have an average thickness of 37.5 km west of the RMF. Relatively thin crust, ~18–32 km, underlies most of the Basin and Range, Salton Trough, Columbia Basin, and along the California coast (Figure 3). Thicker crust, ~42–53 km, underlies the Colorado Plateau, southern Rocky Mountains, the western end of the Wyoming craton-Yavapai Province suture, and the Trans Hudson Orogen (THO). Compared to prior results the THO crust is slightly thinner, with a maximum thickness of ~53 km compared to prior estimates of up to 55–60 km [*Thurner et al.*, 2015; *Shen et al.*, 2013a]. Prior estimates for the western Colorado Plateau vary from ~35 to 58 km [*Levander et al.*, 2011; *Wilson et al.*, 2010; *Bashir et al.*, 2011; *Gilbert*, 2012], and we found a range of ~45–50 km because we interpolated across small areas where the Moho is ambiguous due to multiple weak arrivals. Where denser station spacing exists our results are smoother but otherwise in agreement with regional studies [e.g., *Frassetto et al.*, 2011; *Hansen et al.*, 2013; *Yeck et al.*, 2014; *Gao*, 2015].

Average crustal thickness is greater east of the RMF (42 km) despite lower elevations, and much but not all of the thickest crust lies near Proterozoic to Paleozoic sutures. Crustal thicknesses >47 km were found along the Proterozoic sutures between the Mazatzal and Granite-Rhyolite Provinces, the Superior craton and Yavapai province, and beneath the Llano Front (Figure 3). Proterozoic rifts have varied expressions in modern crust thickness. Locally, thicker crust was found for some segments of the Midcontinent Rift (MCR) [*French et al.*, 2009; *Shen et al.*, 2013b]. Other segments of the MCR and the Oklahoma aulacogen show no clear local thickness variation. Thinner crust, ~32–37 km, underlies the Reelfoot Rift and has a broader extent normal to the strike of the rift, which is geometrically similar to an area of low-velocity upper mantle [*Pollitz and Mooney*, 2014]. Landward of the Gulf of Mexico <40 km thick crust extends to the Precambrian margin

[e.g., *Whitmeyer and Karlstrom*, 2007], except beneath the Reelfoot rift. Crustal thickness of ~35 km near the Gulf Coast is similar to the closest offshore estimate from the northeastern Gulf [*Eddy et al.,* 2014], and ~7 km greater than in the northwestern Gulf [*Van Avendonk et al.,* 2015]. Thicker crust near the northwestern coast is consistent with a recent onshore study [*Agrawal et al.,* 2015].

From the Grenville Front to the Appalachian Piedmont we found ~43–55 km thick crust, which locally agrees with prior studies [*Parker et al.,* 2013; *French et al.,* 2009; *Li et al.,* 2002; *Wagner et al.,* 2012; *Benoit et al.,* 2014]. Thick crust extends southeast of the Blue Ridge province beneath the Piedmont in parts of northern Alabama and Georgia, but from northeastern Georgia to southern Pennsylvania there is a landward increase in thickness at the edge of the Piedmont [*Parker et al.,* 2013; *Cook and Vasudevan*, 2006]. The northeastern Appalachian Mountains crust, east of $-73°$W, is only 32–38 km thick in contrast to the thicker crust farther south. Similarly, the crust east of the Grenville Front in Canada is only 35–42 km thick.

3.2. Contrasting Isostasy Trends East and West of the RMF

Across the contiguous U.S. crust thickness and elevation exhibit a weak Pearson correlation coefficient of $r = 0.14$, but separately, the areas east and west of the RMF exhibit much stronger correlations of $r = 0.61$ and $r = 0.51$, respectively (Figure 3). Accordingly, optimization of Airy isostasy parameters H and $\rho_{um} - \rho_{lc}$ yielded contrasting results. The L1 optimal parameters east of the RMF (AiryE) are $H = 37.5$ km and $\rho_{um} - \rho_{lc} = 0.18$ g/cm^3, and optimal parameters west of the RMF (AiryW) are $H = 28$ km and $\rho_{um} - \rho_{lc} = 0.40$ g/cm^3 (Figures 3d and 3e). Use of ρ_{uc} ranging from 2.4 to 2.8 g/cm^3, rather than assuming 2.6 g/cm^3, would result in $\leq$0.5 km changes to H and $\leq$0.03 g/cm^3 changes to $\rho_{um} - \rho_{lc}$. Use of different topographic smoothing radii from 0 to 40 km would result in $\leq$1 km changes to H and $\leq$0.02 g/cm^3 changes to $\rho_{um} - \rho_{lc}$. Tradeoffs between H and $\rho_{um} - \rho_{lc}$ can be observed in the L1 misfit surfaces (Figure 3). The parameter spaces in which L1 misfit is <30% greater than the minima for the AiryE and AiryW models do not overlap (Figures 3e and 3f). The AiryR misfit map, based on PREM, shows that nearly all areas with misfit < -5 km were found east of the RMF and nearly all areas with misfit >5 km were found west of the RMF (Figure 3b).

3.3. Shear Velocity Structure

Upper crustal V_s, shown as the average from 0 to 11 km depth in Figure 4a, generally delineates sedimentary basins from areas, where bedrock is near the surface. Western U.S. V_s results are similar to *Lin et al.* [2014] so we focus on features farther east. Major low V_s anomalies in the upper crust were found in the Mississippi Embayment, on the western edge of the central Appalachian Mountains, in the Oklahoma aulacogen, the Michigan Basin and in some northern segments of the MCR (Figure 4). These upper crust features are similarly expressed in ~5–10 s phase velocity maps of *Ekström* [2014].

In the middle crust, defined as the upper half of the interval between 11 km and the Moho, we found low V_s (<3.6 km/s) beneath the Mississippi Embayment and along some sections of the southeastern coast. Aside from the Mississippi Embayment, the lowest-V_s areas were found west of the RMF. In the lower crust, defined as the bottom half of the interval between 11 km and the Moho, high V_s (>3.9 km/s) is generally found east of the RMF with only small areas of high V_s west of the RMF. East of the RMF high-velocity lower crust was found in the Reelfoot Rift [*Mooney et al.,* 1983], along the Gulf of Mexico coast, and in the northern Great Plains [*Shen et al.,* 2013a, 2013b]. At uppermost mantle depths (Figure 4d) the passive margin of the eastern and southern U.S. typically has V_s intermediate to the very high V_s (>4.65 km/s) of the cratonic interior and the very low V_s of the western Cordillera (<4.35 km/s).

4. Discussion

4.1. Isostasy East and West of the RMF

The slope of the crust thickness versus elevation trend is dominantly controlled by $\rho_{um} - \rho_{lc}$. The AiryE optimal $\rho_{um} - \rho_{lc}$ of 0.18 g/cm^3 is much lower than the 0.48 g/cm^3 contrast in PREM, but similar to prior regional studies in the central and eastern U.S. [*Li et al.,* 2002; *French et al.,* 2009; *Hawman et al.,* 2012]. Our new results suggest that a similarly small density contrast is required to achieve isostatic balance for most of the area east of the RMF. West of the RMF the optimal $\rho_{um} - \rho_{lc}$ value of 0.39 g/cm^3 is more than double that east of the RMF, but still lower than in PREM. A slightly weaker correlation between crust thickness and elevation west of the RMF ($r = 0.51$) compared to east ($r = 0.61$) indicates that lateral density variations are more prevalent west of the RMF.

The optimal H value of 28.5 km west of the RMF is much lower than global mean continental crust thickness at sea level of ~38 km [*Christensen and Mooney*, 1995] and indicates a long wavelength source of buoyancy. A recent evaluation of potential buoyancy sources for western U.S. topography found an approximately constant uppermost mantle thermal contribution [*Levandowski et al.*, 2014], which we suggest is the primary cause of the low H value. Additional deeper mantle contribution to the low H value is also likely due to mantle flow [*Forte et al.*, 2010; *Liu*, 2015; *Becker et al.*, 2014].

4.2. Implications for the Lower Crust

Both the lower crust and upper mantle affect $\rho_{um} - \rho_{lc}$, but we suggest that the lower crust plays a greater role in the difference across the RMF for two main reasons. First, attempting to account for lower ρ_{um} west of the RMF would only increase the difference in ρ_{lc} needed to explain our results. Second, density variations in the lower crust are expected to be greater than those in the uppermost mantle, despite the fact that peak-to-peak V_s variations in both are ~20% (Figure 4). Much of the low-V_s upper mantle west of the RMF likely contains a contribution from partial melt [*Rau and Forsyth*, 2011; *Schmandt and Humphreys*, 2010], which results in a more modest density effect than subsolidus thermal expansion [*Levandowski et al.*, 2014]. Additionally, high-V_s cratonic upper mantle is likely near neutrally buoyant on account of positive compositional buoyancy that offsets negative thermal buoyancy [*Jordan*, 1988; *Lee et al.*, 2011]. Given these effects and the knowledge that any decrease in ρ_{um} west of the RMF must be balanced by a further decrease in ρ_{lc}, we consider the 0.21 g/cm^3 difference in optimal $\rho_{um} - \rho_{lc}$ for the AiryE and AiryW models an approximate lower bound on the difference in ρ_{lc}.

If, for simplicity, we neglect lateral variations in ρ_{um} and assume a uniform value ranging from 3.30 g/cm^3 for a peridotite model with a warm geotherm [*Afonso et al.*, 2010] to 3.38 g/cm^3 from PREM, then our results would imply mean ρ_{lc} of 3.12–3.20 g/cm^3 and 2.9–2.98 g/cm^3 east and west of the RMF, respectively. The western value is consistent with a wide range of felsic and mafic rocks [*Hacker et al.*, 2015; *Guerri et al.*, 2015]. Densities greater than ~3.15–3.2 g/cm^3 east of the RMF would favor mafic compositions [*Hacker et al.*, 2015], which may have been emplaced in the lower crust near the time of crust formation or during subsequent magmatic events [e.g., *Barnhart et al.*, 2012].

Location of the contrast in isostasy trends (Figure 3) and lower crustal V_s (Figure 4) at the RMF provides an important geologic constraint because the RMF is a Laramide age (~80–40 Ma) boundary that transects multiple Proterozoic sutures (Figure 3b). Hence, the inferred contrast in lower crust density is a product of Laramide to post-Laramide processes rather than Precambrian inheritance. Hydration of the lithosphere during Laramide flat slab subduction and heating during subsequent magmatism likely reduced the density of lower crust [*Humphreys et al.*, 2003; *Jones et al.*, 2015]. Some dense lower crust may also have been removed by delamination or Rayleigh-Taylor instability [e.g., *Zandt et al.*, 2004; *Hales et al.*, 2005; *Levander et al.*, 2011].

4.3. Contrasting Orogenic Systems

Multiple Proterozoic to Paleozoic orogens maintain >45 km thick high-velocity crust (Figure 3), but it does not appear possible for the active southern or northern Rocky Mountains to leave a similar structural record if they were to evolve in the absence of further tectonic deformation and magmatism. Modern crustal thicknesses of the southern and northern Rocky Mountains are less than or similar to those found near in areas of Grenville and Appalachian deformation (Figure 3), yet their elevations are ~2 km greater and continued erosion and exhumation is expected to thin the crust. This difference may stem from the fact that much of the Cretaceous to present orogeny occurred far from the plate margin and involved little accretion. Mantle-driven thermal and compositional increases in buoyancy were likely more important to uplift of the Rocky Mountains than crustal shortening [*Humphreys et al.*, 2003; *Jones et al.*, 2015; *Karlstrom et al.*, 2012]. In contrast, Proterozoic to Paleozoic orogens that maintain thick high-V_s crustal roots were associated with shortening and stacking of newly accreted and preexisting crust [e.g., *Whitmeyer and Karlstrom*, 2007; *Hatcher*, 2010].

5. Concluding Remarks

Our results show that the RMF separates areas of North America crust that exhibit contrasting crust thickness versus elevation trends. The difference in trend slopes is primarily attributed to contrasting lower crustal density. The mean lower crust to upper mantle density contrast inferred for the area east of the RMF is about

half of that west of the RMF. Location of the contrast in crustal character at the RMF suggests Laramide to post-Laramide alteration reduced the density of the western U.S. lower crust.

References

Afonso, J. C., G. Ranalli, M. Fernàndez, W. L. Griffin, S. Y. O'Reilly, and U. Faul (2010), On the Vp/Vs–Mg# correlation in mantle peridotites: Implications for the identification of thermal and compositional anomalies in the upper mantle, *Earth Planet. Sci. Lett.*, *289*(3), 606–618.

Agrawal, M., J. Pulliam, M. K. Sen, and H. Gurrola (2015), Lithospheric structure of the Texas-Gulf of Mexico passive margin from surface wave dispersion and migrated Ps receiver functions, *Geochem. Geophys. Geosyst.*, *16*, 2221–2239, doi:10.1002/2015GC005803.

Amante, C., and B. W. Eakins (2009), ETOPO1 1 arc-minute global relief model: procedures, data sources and analysis, pp. 19, U.S. Dep. of Commer., Natl. Oceanic and Atmos. Admin., Natl. Environ. Satell., Data, and Inf. Serv., Natl. Geophys. Data Cent, Mar. Geol. and Geophys. Div.

Angus, D. A., J. M. Kendall, D. C. Wilson, D. J. White, S. Sol, and C. J. Thomson (2009), Stratigraphy of the Archean western Superior Province from P-and S-wave receiver functions: Further evidence for tectonic accretion?, *Phys. Earth Planet. Inter.*, *177*(3), 206–216.

Barnhart, K. R., K. H. Mahan, T. J. Blackburn, S. A. Bowring, and F. O. Dudas (2012), Deep crustal xenoliths from central Montana, USA: Implications for the timing and mechanisms of high-velocity lower crust formation, *Geosphere*, *8*(6), 1408–1428.

Bashir, L., S. S. Gao, K. H. Liu, and K. Mickus (2011), Crustal structure and evolution beneath the Colorado Plateau and the southern Basin and Range Province: Results from receiver function and gravity studies, *Geochem. Geophys. Geosyst.*, *12*, Q06008, doi:10.1029/2011GC003563.

Beck, S. L., G. Zandt, S. C. Myers, T. C. Wallace, P. G. Silver, and L. Drake (1996), Crustal-thickness variations in the central Andes, *Geology*, *24*(5), 407–410.

Becker, T. W., C. Faccenna, E. D. Humphreys, A. R. Lowry, and M. S. Miller (2014), Static and dynamic support of western United States topography, *Earth Planet. Sci. Lett.*, *402*, 234–246.

Benoit, M. H., C. Ebinger, and M. Crampton (2014), Orogenic bending around a rigid Proterozoic magmatic rift beneath the Central Appalachian Mountains, *Earth Planet. Sci. Lett.*, *402*, 197–208.

Bensen, G. D., M. H. Ritzwoller, M. P. Barmin, A. L. Levshin, F. Lin, M. P. Moschetti, N. M. Shapiro, and Y. Yang (2007), Processing seismic ambient noise data to obtain reliable broad-band surface wave dispersion measurements, *Geophys. J. Int.*, *169*(3), 1239–1260.

Blackwell, D. D., P. T. Negraru, and M. C. Richards (2006), Assessment of the enhanced geothermal system resource base of the United States, *Nat. Resour. Res.*, *15*(4), 283–308.

Brocher, T. M. (2005), Empirical relations between elastic wave speeds and density in the Earth's crust, *Bull. Seismol. Soc. Am.*, *95*(6), 2081–2092.

Christensen, N., and W. Mooney (1995), Seismic velocity structure and composition of the continental crust: A global view, *J. Geophys. Res.*, *100*, 9761–9788.

Cook, F. A., and K. Vasudevan (2006), Reprocessing and enhanced interpretation of the initial COCORP Southern Appalachians traverse, *Tectonophysics*, *420*(1), 161–174.

Dueker, K. G., and A. F. Sheehan (1997), Mantle discontinuity structure from midpoint stacks of converted P to S waves across the Yellowstone hotspot track, *J. Geophys. Res.*, *102*, 8313–8327.

Dziewonski, A. M., and D. L. Anderson (1981), Preliminary reference Earth model, *Phys. Earth Planet. Inter.*, *25*(4), 297–356.

Eagar, K. C., M. J. Fouch, D. E. James, and R. W. Carlson (2011), Crustal structure beneath the High Lava Plains of eastern Oregon and surrounding regions from receiver function analysis, *J. Geophys. Res.*, *116*, B02313, doi:10.1029/2010JB007795.

Eddy, D. R., H. J. Van Avendonk, G. L. Christeson, I. O. Norton, G. D. Karner, C. A. Johnson, and J. W. Snedden (2014), Deep crustal structure of the northeastern Gulf of Mexico: Implications for rift evolution and seafloor spreading, *J. Geophys. Res. Solid Earth*, *119*, 6802–6822, doi:10.1002/2014JB011311.

Ekström, G. (2014), Love and Rayleigh phase-velocity maps, 5–40 s, of the western and central USA from USArray data, *Earth Planet. Sci. Lett.*, *402*, 42–49.

Fenneman, N. M. (1928), Physiographic divisions of the United States, *Ann. Assoc. Am. Geogr.*, *18*(4), 261–353.

Fischer, K. M. (2002), Waning buoyancy in the crustal roots of old mountains, *Nature*, *417*(6892), 933–936.

Forte, A. M., R. Moucha, N. A. Simmons, S. P. Grand, and J. X. Mitrovica (2010), Deep-mantle contributions to the surface dynamics of the North American continent, *Tectonophysics*, *481*(1), 3–15.

Frassetto, A. M., G. Zandt, H. Gilbert, T. J. Owens, and C. H. Jones (2011), Structure of the Sierra Nevada from receiver functions and implications for lithospheric foundering, *Geosphere*, *7*(4), 898–921.

French, S. W., K. M. Fischer, E. M. Syracuse, and M. E. Wysession (2009), Crustal structure beneath the Florida-to-Edmonton broadband seismometer array, *Geophys. Res. Lett.*, *36*, L08309, doi:10.1029/2008GL036331.

Gao, H. (2015), Crustal seismic structure beneath the source area of the Columbia River flood basalt: Bifurcation of the Moho driven by lithosphere delamination, *Geophys. Res. Lett.*, doi:10.1002/2015GL066625.

Gilbert, H. (2012), Crustal structure and signatures of recent tectonism as influenced by ancient terranes in the western United States, *Geosphere*, *8*(1), 141–157.

Guerri, M., F. Cammarano, and J. A. Connolly (2015), Effects of chemical composition, water and temperature on physical properties of continental crust, *Geochem. Geophys. Geosyst.*, *16*, 2431–2449, doi:10.1002/2015GC005819.

Hacker, B. R., P. B. Kelemen, and M. D. Behn (2015), Continental lower crust, *Annu. Rev. Earth Planet. Sci.*, *43*, 167–205.

Hales, T. C., D. L. Abt, E. D. Humphreys, and J. J. Roering (2005), A lithospheric instability origin for Columbia River flood basalts and Wallowa Mountains uplift in northeast Oregon, *Nature*, *438*(7069), 842–845.

Hansen, S., and K. Dueker (2009), P-and S-wave receiver function images of crustal imbrication beneath the Cheyenne Belt in southeast Wyoming, *Bull. Seismol. Soc. Am.*, *99*(3), 1953–1961.

Hansen, S. M., K. G. Dueker, J. C. Stachnik, R. C. Aster, and K. E. Karlstrom (2013), A rootless rockies—Support and lithospheric structure of the Colorado Rocky Mountains inferred from CREST and TA seismic data, *Geochem. Geophys. Geosyst.*, *14*, 2670–2695, doi:10.1002/ggge.20143.

Hatcher, R. D., Jr. (2010), The Appalachian orogen: A brief summary, in *From Rodinia to Pangea: The Lithotectonic Record of the Appalachian Region*, *Geol. Soc. Am. Mem.*, vol. 206, edited by R. P. Tollo et al., pp. 1–19, Geol. Soc. Am., Boulder, Colo.

Hawman, R. B., M. O. Khalifa, and M. S. Baker (2012), Isostatic compensation for a portion of the Southern Appalachians: Evidence from a reconnaissance study using wide-angle, three-component seismic soundings, *Geol. Soc. Am. Bull.*, *124*(3-4), 291–317.

Humphreys, E., E. Hessler, K. Dueker, G. L. Farmer, E. Erslev, and T. Atwater (2003), How Laramide-age hydration of North American lithosphere by the Farallon slab controlled subsequent activity in the western United States, *Int. Geol. Rev.*, *45*(7), 575–595.

Jones, C. H., K. H. Mahan, L. A. Butcher, W. B. Levandowski, and G. L. Farmer (2015), Continental uplift through crustal hydration, *Geology*, *43*(4), 355–358.

Jordan, T. H. (1988), Structure and formation of the continental tectosphere, *J. Petrol.*, (1), 11–37.

Karlstrom, K. E., et al. (2012), Mantle-driven dynamic uplift of the Rocky Mountains and Colorado Plateau and its surface response: Toward a unified hypothesis, *Lithosphere*, *4*(1), 3–22.

Kim, Y., M. S. Miller, F. Pearce, and R. W. Clayton (2012), Seismic imaging of the Cocos plate subduction zone system in central Mexico, *Geochem. Geophys. Geosyst.*, *13*, Q07001, doi:10.1029/2012GC004033.

Laske, G., G. Masters, Z. Ma, and M. Pasyanos (2013), Update on CRUST1.0—A 1-degree global model of Earth's crust, *Geophys. Res. Abstr.*, *15*, Abstract EGU2013-2658.

Lee, C. T. A., P. Luffi, and E. J. Chin (2011), Building and destroying continental mantle, *Annu. Rev. Earth Planet. Sci.*, *39*, 59–90.

Levander, A., and M. S. Miller (2012), Evolutionary aspects of lithosphere discontinuity structure in the western US, *Geochem. Geophys. Geosyst.*, *13*, Q0AK07, doi:10.1029/2012GC004056.

Levander, A., B. Schmandt, M. S. Miller, K. Liu, K. E. Karlstrom, R. S. Crow, C.-T. Lee, and E. D. Humphreys (2011), Continuing Colorado plateau uplift by delamination-style convective lithospheric downwelling, *Nature*, *472*(7344), 461–465.

Levandowski, W., C. H. Jones, W. Shen, M. H. Ritzwoller, and V. Schulte-Pelkum (2014), Origins of topography in the western US: Mapping crustal and upper mantle density variations using a uniform seismic velocity model, *J. Geophys. Res. Solid Earth*, *119*, 2375–2396, doi:10.1002/2013JB010607.

Li, A., K. M. Fischer, S. van der Lee, and M. E. Wysession (2002), Crust and upper mantle discontinuity structure beneath eastern North America, *J. Geophys. Res.*, *107*(B5), 2100, doi:10.1029/2001JB000190.

Lin, F. C., and M. H. Ritzwoller (2011), Helmholtz surface wave tomography for isotropic and azimuthally anisotropic structure, *Geophys. J. Int.*, *186*(3), 1104–1120.

Lin, F. C., M. H. Ritzwoller, and R. Snieder (2009), Eikonal tomography: Surface wave tomography by phase front tracking across a regional broad-band seismic array, *Geophys. J. Int.*, *177*(3), 1091–1110.

Lin, F. C., B. Schmandt, and V. C. Tsai (2012), Joint inversion of Rayleigh wave phase velocity and ellipticity using USArray: Constraining velocity and density structure in the upper crust, *Geophys. Res. Lett.*, *39*, L12303, doi:10.1029/2012GL052196.

Lin, F. C., V. C. Tsai, and B. Schmandt (2014), 3-D crustal structure of the western United States: Application of Rayleigh-wave ellipticity extracted from noise cross-correlations, *Geophys. J. Int.*, *198*, 656–670.

Liu, L. (2015), The ups and downs of North America: Evaluating the role of mantle dynamic topography since the Mesozoic, *Rev. Geophys.*, *53*, 1022–1049, doi:10.1002/2015RG000489.

Lowry, A. R., and M. Pérez-Gussinyé (2011), The role of crustal quartz in controlling Cordilleran deformation, *Nature*, *471*(7338), 353–357.

MacKenzie, L. S., G. A. Abers, S. Rondenay, and K. M. Fischer (2010), Imaging a steeply dipping subducting slab in Southern Central America, *Earth Planet. Sci. Lett.*, *296*(3), 459–468.

Mercier, J. P., M. G. Bostock, and A. M. Baig (2006), Improved Green's functions for passive-source structural studies, *Geophysics*, *71*(4), SI95–SI102.

Mooney, W. D., M. C. Andrews, A. Ginzburg, D. A. Peters, and R. M. Hamilton (1983), Crustal structure of the northern Mississippi embayment and a comparison with other continental rift zones, *Tectonophysics*, *94*(1), 327–348.

Parker, E. H., R. B. Hawman, K. M. Fischer, and L. S. Wagner (2013), Crustal evolution across the southern Appalachians: Initial results from the SESAME broadband array, *Geophys. Res. Lett.*, *40*, 3853–3857, doi:10.1002/grl.50761.

Pollitz, F. F., and W. D. Mooney (2014), Seismic structure of the Central US crust and shallow upper mantle: Uniqueness of the Reelfoot Rift, *Earth Planet. Sci. Lett.*, *402*, 157–166.

Rau, C. J., and D. W. Forsyth (2011), Melt in the mantle beneath the amagmatic zone, southern Nevada, *Geology*, *39*(10), 975–978.

Schmandt, B., and E. Humphreys (2010), Complex subduction and small-scale convection revealed by body-wave tomography of the western United States upper mantle, *Earth Planet. Sci. Lett.*, *297*(3), 435–445.

Schmandt, B., and F. C. Lin (2014), P and S wave tomography of the mantle beneath the United States, *Geophys. Res. Lett.*, *41*, 6342–6349, doi:10.1002/2014GL061231.

Schmandt, B., K. Dueker, E. Humphreys, and S. Hansen (2012), Hot mantle upwelling across the 660 beneath Yellowstone, *Earth Planet. Sci. Lett.*, *331*, 224–236.

Sheehan, A. F., G. A. Abers, C. H. Jones, and A. L. Lerner-Lam (1995), Crustal thickness variations across the Colorado Rocky Mountains from teleseismic receiver functions, *J. Geophys. Res.*, *100*, 20,391–20,404.

Shen, W., M. H. Ritzwoller, and V. Schulte-Pelkum (2013a), A 3-D model of the crust and uppermost mantle beneath the Central and Western US by joint inversion of receiver functions and surface wave dispersion, *J. Geophys. Res. Solid Earth*, *118*, 262–276, doi:10.1029/2012JB009602.

Shen, W., M. H. Ritzwoller, and V. Schulte-Pelkum (2013b), Crustal and uppermost mantle structure in the central US encompassing the Midcontinent Rift, *J. Geophys. Res. Solid Earth*, *118*, 4325–4344, doi:10.1002/jgrb.50321.

Tanimoto, T., and L. Rivera (2008), The ZH ratio method for long-period seismic data: Sensitivity kernels and observational techniques, *Geophys. J. Int.*, *172*(1), 187–198.

Thurner, S., R. Margolis, A. Levander, and F. Niu (2015), PdS receiver function evidence for crustal scale thrusting, relic subduction, and mafic underplating in the Trans-Hudson Orogen and Yavapai province, *Earth Planet. Sci. Lett.*, *426*, 13–22.

Van Avendonk, H. J., G. L. Christeson, I. O. Norton, and D. R. Eddy (2015), Continental rifting and sediment infill in the northwestern Gulf of Mexico, *Geology*, *43*(7), 631–634.

Wagner, L. S., K. Stewart, and K. Metcalf (2012), Crustal-scale shortening structures beneath the Blue Ridge Mountains, North Carolina, USA, *Lithosphere*, *4*(3), 242–256.

Whitmeyer, S. J., and K. E. Karlstrom (2007), Tectonic model for the Proterozoic growth of North America, *Geosphere*, *3*(4), 220–259.

Wilson, D., and R. Aster (2005), Seismic imaging of the crust and upper mantle using regularized joint receiver functions, frequency–wave number filtering, and multimode Kirchhoff migration, *J. Geophys. Res.*, *110*, B05305, doi:10.1029/2004JB003430.

Wilson, D. C., R. Aster, S. Grand, J. Ni, and W. S. Baldridge (2010), High-resolution receiver function imaging reveals Colorado Plateau lithospheric architecture and mantle-supported topography, *Geophys. Res. Lett.*, *37*, L20313, doi:10.1029/2010GL044799.

Yeck, W. L., A. F. Sheehan, M. L. Anderson, E. A. Erslev, K. C. Miller, and C. S. Siddoway (2014), Structure of the Bighorn Mountain region, Wyoming, from teleseismic receiver function analysis: Implications for the kinematics of Laramide shortening, *J. Geophys. Res. Solid Earth*, *119*, 7028–7042, doi:10.1002/2013JB010769.

Zandt, G., H. Gilbert, T. J. Owens, M. Ducea, J. Saleeby, and C. H. Jones (2004), Active foundering of a continental arc root beneath the southern Sierra Nevada in California, *Nature*, *431*(7004), 41–46.